Acquisition of the Spindle Assembly Checkpoint and its modulation by cell fate and cell size in a chordate embryo

Short title: Spindle Assembly Checkpoint acquisition and modulation in a chordate embryo

Marianne Roca[1,2], Lydia Besnardeau[1], Elisabeth Christians[1], Alex McDougall[1], Janet Chenevert[1*], Stefania Castagnetti[1*]

[1] Sorbonne Universités, CNRS, Laboratoire de Biologie du Développement de Villefranche-sur-Mer (LBDV), 06230 Villefranche-sur-Mer, France.

[2] current address: Max Planck Research Group Genetics of Behavior, Max Planck Institute for Neurobiology of Behavior – Caesar, Ludwig-Erhard-Allee 2, Bonn 53175, Germany

* corresponding authors: castagnetti@imev-mer.fr

Keyword: mitosis, ascidian, spindle assembly checkpoint, embryo, SAC acquisition, kinetochore

Abstract

The spindle assembly checkpoint (SAC) is a surveillance system which preserves genome integrity by delaying anaphase onset until all chromosomes are correctly attached to spindle microtubules. Recruitment of SAC proteins to unattached kinetochores generates an inhibitory signal that prolongs mitotic duration. Chordate embryos are atypical in that spindle defects do not delay mitotic progression during early development, implying that either the SAC is inactive or the cell-cycle target machinery unresponsive. Here we show that in embryos of the chordate *Phallusia mammillata* the SAC delays mitotic progression from the 8th cleavage divisions. Unattached kinetochores are not recognized by the SAC machinery until the 7th cell cycle when the SAC is acquired. Following acquisition, SAC strength, manifest as the degree of mitotic lengthening induced by spindle perturbations, is specific to different cell types and is modulated by cell size showing similarity to SAC control in early *Caenorhabditis elegans* embryos. We conclude that SAC acquisition is a process likely specific to chordate embryos,

while modulation of SAC efficiency in SAC proficient stages depends on cell fate and cell size similarly to non-chordate embryos.

Introduction

The spindle assembly checkpoint (SAC) operates during mitosis to ensure fidelity of chromosome segregation and loss of SAC function is often associated with chromosome segregation errors and the generation of daughter cells with an abnormal chromosome number, a condition called aneuploidy, deleterious for cell viability and organismal survival (Chunduri and Storchová, 2019). The SAC monitors kinetochore-spindle microtubule attachments through the recruitment of SAC components to unattached kinetochores until all kinetochores have acquired proper bipolar attachments to spindle microtubules (Jia et al., 2013; Musacchio and Salmon, 2007). Kinetochore localization of SAC proteins promotes the formation of a soluble complex, the mitotic checkpoint complex, which by sequestering Cdc20 acts as a potent inhibitor of APC/C (an E3 ubiquitin ligase required for anaphase onset and mitotic exit) delaying chromosome segregation and mitotic progression (De Antoni et al., 2005; Sudakin et al., 2001).

Even though the SAC is essential to preserve ploidy, the response to spindle defects varies across cell types, and early embryos of several species dispense with the SAC (Chenevert et al., 2020). This variability in SAC efficiency has been attributed to differences in cell size and cell identity. However, the available results are contradictory. Studies carried out in *C. elegans* embryos showed that the SAC becomes more efficient, delaying mitosis for longer, at each division following fertilization, as cell volume is reduced (Galli and Morgan, 2016; Gerhold et al., 2018). These data can be explained by a modulation model whereby SAC signal generated at kinetochores is diluted in the cytoplasm and the strength of SAC response is influenced by kinetochore-to-cytoplasmic ratio. Consistent with this notion, in *Xenopus* egg extracts, the mitotic checkpoint can be activated by increasing the concentration of added sperm heads (Minshull et al., 1994) and in mouse reduction of oocyte size results in a stronger SAC response during meiosis (Kyogoku and Kitajima, 2017; Lane et al., 2017). Crucially however, artificially changing cell volume does not affect the timing of SAC acquisition either in frog (Clute and Masui, 1995; Clute and Masui, 1997) or in fish embryos (Zhang et al., 2015), suggesting that modulation of SAC strength and SAC acquisition might be two different phenomena.

67 It has proven difficult to tease apart SAC acquisition from SAC modulation. However,
68 a prerequisite of the modulation hypothesis is that SAC proteins do accumulate on unattached
69 kinetochores but the inhibitory signal produced is too weak to induce a delay in mitotic
70 progression. In SAC-proficient *C. elegans* embryos, Mad1 and Mad2 localize to unattached
71 kinetochores already from the 2-cell stage (Galli and Morgan 2016). Kinetochore localization
72 of SAC components has not been analysed in SAC-deficient fish and frog embryos. However,
73 in embryos of the ascidian *Phallusia mammillata* Mps1, Mad2 and Mad1 do not accumulate to
74 unattached kinetochores in 2-cell stage embryos (Chenevert et al., 2020).
75 Here we find that in *P. mammillata* embryos the SAC becomes efficient at the 8th cell
76 cycle. The appearance of a functional SAC correlates with SAC acquisition rather than SAC
77 modulation since recruitment of SAC proteins to unattached kinetochores first occurs at the 7th
78 cell cycle. We show that, following SAC acquisition SAC strength increases at each cell
79 division and is influenced by cell identity, similarly to SAC proficient non-chordate embryos
80 (Gerhold et al., 2018). We suggest that within same-fated cells SAC strength is then modulated
81 by changes in cell size. In the ventral ectoderm, the difference in SAC activity observed
82 between anterior and posterior cells requires GSK3 activity to enhance SAC strength in anterior
83 cells. Although SAC acquisition appears to be specific to chordate embryos (Chenevert et al.,
84 2020), SAC modulation in chordates depends on cell fate and cell size similarly to non-chordate
85 embryos.
86
87 **Results and Discussion**
88 We previously showed that the SAC is inefficient in *P. mammillata* 2-cell stage embryos
89 where nocodazole treatment prevents spindle formation, but induces only a limited mitotic
90 delay (Chenevert et al., 2020). To determine when the SAC becomes functional in *P.*
91 *mammillata* embryos, we analyzed mitotic duration in the absence of spindle microtubules (Fig.
92 S1), from the 2nd to 10th cell cycle following fertilization. Mitotic duration was measured as the
93 time spent between nuclear envelope breakdown (NEB), and nuclear envelope reformation
94 (NER; Fig. 1A). Consistent with earlier studies (Dumollard et al., 2017), mitotic duration in
95 control embryos (DMSO) was constant at all analyzed stages (Fig. 1B) and lasted on average
96 10 minutes. As for 2-cell stage embryos (Chenevert et al., 2020), mitotic duration was briefly
97 extended in 4- to 64-cell stage embryos treated with nocodazole, compared to DMSO-treated
98 embryos (1.5-fold) (Fig. 1B). From the 8th cell cycle, however, in nocodazole-treated embryos
99 mitotic duration was prolonged more extensively at each cell cycle, extending by 2.5-fold
100 (24.5±8.5 minutes) at the 8th cycle (128-cell), by 4.5-fold (37.3±14.5 minutes) at the 9th cycle

101 (256-cells) and by 6.5-fold (64.3±20 minutes) at the 10th cycle (512-cells). To determine whether
102 this mitotic delay required SAC activity, we then measured mitotic duration in the presence of
103 nocodazole in SAC impaired embryos (Fig. 2A). Mutations of three phosphorylation sites in
104 the human SAC protein Mad2 produce a dominant negative form of Mad2 (Mad2-DN) that
105 impairs SAC activity (Fig. S2A) (Wassmann et al., 2003a; Wassmann et al., 2003b). We tested
106 the effect of Mad2-DN on mitotic duration during *P. mammillata* development. At the 2-cell
107 stage, overexpression of Mad2-DN did not affect mitotic duration, either in the presence (Fig.
108 S2B) or in the absence (Fig. 2B) of microtubules. However, both at the 8th and the 9th cell cycles
109 mitotic duration in the presence of nocodazole was significantly reduced by Mad2-DN
110 overexpression (Fig. 2B) lasting only 1.5 times longer in nocodazole-treated than in DMSO-
111 treated embryos (128-cell: DMSO = 9.8±1.6 to nocodazole = 15.6±3.5 minutes; 256-cell:
112 9.9±1.8 to 13.6±2.4 minutes), comparable to mitotic duration in nocodazole treated wild-type
113 early embryos (2- to 64- cells). Similarly impairing SAC activity with reversine, a specific
114 inhibitor of Mps1, the kinase that initiates the SAC signaling cascade (Fig. 2A)(Santaguida et
115 al., 2010), prevents mitotic lengthening following nocodazole treatment at the 9th cell cycle (Fig.
116 2B). Hence, the SAC is required to delay mitotic exit from the 8th cell cycle. During the first
117 seven cell division cycles the SAC could either be inactive, or active but unable to induce a
118 prolonged delay in mitotic duration.
119 To distinguish between these two hypotheses, we assessed whether a SAC signal was
120 produced during the early division cycles. As kinetochore localization of SAC components is
121 an essential prerequisite for SAC signaling (Musacchio and Salmon, 2007), we analyzed the
122 presence of Mad1 throughout development and its localization to unattached kinetochores,
123 before and after SAC acquisition, using a specific antibody against *P. mammillata* Mad1
124 (Chenevert et al., 2020). We find that Mad1 protein is present at similar levels throughout
125 development (Fig. 2C) irrespective of SAC activity. As for yeast and somatic cells (Rodriguez-
126 Bravo et al., 2014), Mad1 localizes to the nuclear envelope during interphase at all
127 developmental stages independently of microtubules (Fig. 2D and S2C). However, as for 2-cell
128 stage embryos (Chenevert et al., 2020), in the presence of nocodazole, Mad1 does not
129 accumulate to mitotic chromosomes in 4- to 32- cell embryos (Fig. 2D). Mad1 foci associated
130 with mitotic chromosomes were observed in 128- and 256-cell stage embryos (53% and 74%
131 of mitotic cells respectively). We also observed weak accumulation of Mad1 on unattached
132 chromosomes in 14% of mitotic cells at the 64-cell stage (Fig. 2D). It is thus possible to
133 distinguish two phases during *P. mammillata* development with respect to SAC activity; first,
134 a SAC-deficient phase when the presence of unattached kinetochores goes undetected by the

135 cell, which continues cycling irrespective of the lack of spindle-kinetochore interactions, and
136 second a SAC-proficient phase when the SAC machinery is recruited to unattached
137 kinetochores, an essential step in the generation of the inhibitory signal that delays mitotic
138 progression until the formation of correct bipolar interactions.
139
140 After the 8th cell cycle, SAC response increases both in strength and variability at each
141 cell cycle (Fig. 1B). At this stage, most cells in the ascidian embryo are fate-restricted. We then
142 asked whether SAC strength is a property of different cell identities and analyzed SAC strength
143 in different cell populations. We observed that at the 9th cell cycle, in the presence of nocodazole,
144 cells of the anterior ventral ectoderm spent significantly longer in mitosis than cells of the
145 posterior ventral ectoderm, dorsal ectoderm or notochord (Fig. 3A, B).
146 To dissect what influences this difference in SAC strength we focused on the ventral
147 ectoderm as those cells are easily accessible on the surface of the embryo, and two SAC
148 behaviors can be observed in the same field of view. We first asked whether the difference
149 between these two populations could be explained by a difference in cell size. Using the
150 membrane marker PH-GFP, we measured cell volume and observed a similar range of cell
151 volumes for anterior and posterior ventral ectodermal cells (Fig. 3C), excluding that the
152 difference in mitotic response between these two cell populations is due to a difference in cell
153 size.
154 We then asked whether the difference in SAC strength along the antero-posterior axis
155 is a consequence of the difference in cell fates. We therefore interfered with patterning along
156 the anterior-posterior axis and analyzed SAC strength at the 9th cell cycle. In the ascidian *Ciona*
157 *intestinalis*, GSK3 is active in anterior cells and its inhibition from the onset of gastrulation
158 results in loss of anterior identity in the ectoderm with extension of the posterior domain
159 (Feinberg et al., 2019). We observed a similar effect in *P. mammillata* embryos treated with the
160 specific GSK3 inhibitor BIO from the onset of gastrulation (Fig. 3D). BIO-treated embryos did
161 not express the anterior markers *FoxF* (Fig. 3E) (Feinberg et al., 2019)) and *sFRP1/5* (Fig.
162 S3A) (Lamy et al., 2006), and developed into tadpoles with diminished anterior structures (Fig.
163 3E), consistent with the acquisition of posterior identity in the anterior ventral ectoderm. At the
164 256-cell stage, BIO-treated embryos maintained their overall shape, allowing orientation of the
165 embryo along the anterior-posterior axis (Fig. 3E). At this stage, mitotic duration was slightly
166 extended in posterior ectodermal cells by BIO treatment alone, but no effect was observed in
167 anterior ectodermal cells (Fig. S3B; wild-type: anterior 11.8±2.9 minutes, posterior 10.7±1
168 minutes; BIO: anterior 12.1±2.9 minutes, posterior 13.6±3.2 minutes). In the presence of

169 nocodazole, however, (Fig. 3F) mitotic duration was significantly shorter in anterior cells of
170 the ventral ectoderm in BIO-treated embryos than in untreated embryos (untreated: 66.4±19.1
171 minutes, BIO: 50.9±13.9 minutes), while no difference was observed in ventral posterior
172 ectodermal cells (untreated: 44.7±15.2 minutes, BIO: 43.1±11.3 minutes).

173 As posteriorization of anterior cells results in reduction of SAC strength we then asked
174 whether anteriorization of the posterior ectoderm would result in enhancement of SAC
175 efficiency. In *C. intestinalis* the transcription factor FoxA-a is necessary for the acquisition of
176 anterior ectodermal identity and its overexpression in animal blastomeres from the 16-cell stage
177 results in posterior cells acquiring anterior identity (Lamy et al., 2006). To induce anterior fate
178 in the posterior part of the ventral ectoderm we injected *P. mammillata* eggs with a plasmid
179 encoding FoxA-a under the control of the Fog promoter (pFog>FoxA-a) to drive FoxA-a
180 expression in all animal cells (Lamy et al., 2006). At the 9th cell cycle, in pFog>FoxA-a injected
181 embryos expression of the anterior marker *sFRP1/5*, normally restricted to the anterior pole
182 (Fig. S3C), was extended towards the posterior pole in 34% of embryos and was expressed in
183 all cells in 66% of embryos. The latter did not elongate at the neurula stage but developed into
184 round embryos, indicating complete loss of anterior-posterior patterning. At the 9th cell cycle,
185 mitotic duration was unaffected in pFog>FoxA-a-injected embryos in the presence of DMSO
186 (Fig. S3D). In nocodazole-treated round pFog>FoxA-a-injected embryos (Fig. 3G) mitotic
187 duration was extended by 4.4-fold (11.1±2.6 to 48±21.7 minutes), an increase similar to that
188 observed in anterior wild-type cells (9.9±2.4 to 49.3±11.9 minutes). To confirm that
189 anteriorization of the posterior ectoderm results in an increase in SAC strength, we also
190 removed the vegetal pole of fertilized eggs, which contains the maternal factors required for
191 cell differentiation and for the invariant cleavage pattern typical of ascidian development (Fig.
192 4A). Such manipulation of the zygote (pole-ablated) gives rise to embryos in which all cells
193 acquire the anterior ectodermal fate (Dumollard et al., 2017; Nishida, 1996), as shown by
194 ectopic expression of the anterior marker *sFRP1/5* throughout the embryo (Fig. S3C). Pole-
195 ablated embryos acquire SAC activity at the 8th cell cycle and in the presence of nocodazole
196 delay mitotic duration by 2.4-fold (DMSO: 10.7±2.9 to nocodazole: 24.3±7.5 minutes), like
197 ventral ectodermal cells in un-manipulated embryos (Fig. S3E). At the 9th cell cycle, we
198 observed greater variability in mitotic duration in pole-ablated embryos than in anterior
199 ectodermal cells of wild-type embryos, with several cells exhibiting only a short mitotic delay
200 (Fig. 4B). However, we noticed that differently from unmanipulated control embryos where the
201 cell volume of anterior ectodermal cells ranges between $2x10^3$ μm^3 and $4x10^3$ μm^3, in pole-
202 ablated embryos cell volume varied between $1.8x10^3$ μm^3 and $8x10^3$ μm^3 (Fig. 4C). The mitotic

203 delay induced by nocodazole was comparable in control (48±11.9 minutes) and pole ablated
204 (43.5±15.6 minutes) embryos when considering only cells whose volume was comparable
205 (volume <$4x10^3$ μm^3), while in pole ablated cells larger than $4x10^3 \mu m^3$ the mitotic delay was
206 significantly shorter (25.3±6.9 minutes, 2.2-fold increase; Fig. 4C, D). Hence, the difference in
207 SAC efficiency between anterior and posterior ectodermal cells could be attributed to a
208 difference in cell identity. Our data also suggest that within same fated cells, the SAC response
209 is modulated by cell size and is stronger in smaller cells.

210 Thus, following SAC acquisition, SAC strength is specific to different cell populations
211 and is modulated by cell size. This is similar to what was reported for early *C. elegans* embryos,
212 where SAC strength increases at each cleavage division (Galli and Morgan, 2016), in a lineage
213 specific manner (Gerhold et al., 2018). Modulation of SAC strength in SAC proficient cells,
214 therefore, appears to follow similar rules in both chordate and non-chordate embryos. Our
215 results also suggest that GSK3 is involved in enhancing SAC efficiency in anterior ectodermal
216 cells. GSK3 activity as a SAC enhancing factor could be direct through phosphorylation of the
217 SAC machinery and/or the kinetochores to favor their interaction, or indirect through ß-catenin
218 mediated transcriptional control of SAC regulators. Although further work will be required to
219 distinguish between these possibilities, a study carried out in mammalian cells showed that
220 GSK3 promotes the recruitment of the SAC components Mad2, Bub1 and BubR1 to unattached
221 kinetochores and favors the formation of the inhibitory complex (Rashid et al., 2018),
222 supporting a direct role of GSK3 in increasing SAC strength.

223

224 **Material and Methods**

225 **Gamete preparation**

226 All experiments were performed using the ascidian *Phallusia mammillata*, a marine
227 chordate. Animals were collected at Sète (France) and maintained in aquaria at the Laboratoire
228 de Biologie du Developpment de Villefranche sur mer (LBDV).

229 Dissection of adult animals allowed collection of both sperm and eggs. Dry sperm was
230 kept at 4°C for a maximum of 2 weeks. Eggs were collected in microfiltered sea water (MFSW)
231 containing 5 mM TAPS ([tris(hydroxymethyl)methylamino]propanesulfonic acid), pH 8.2
232 (McDougall et al., 2015). The chorion was removed by treatment with 0.1% trypsin in 10 ml
233 MFSW-TAPS for 1.5-2 hours at room temperature (Sardet et al., 1989) . Dechorionated eggs
234 were washed in MFSW and kept at 18°C in MFSW with TAPS. Eggs were used within 36 hours

235 from collection. All glass- and plastic-ware for embryo handling was coated with 0.1% gelatin
236 and 0.1% formaldehyde (GF) (McDougall et al., 2015).
237 Prior to fertilization sperm was activated by incubating 9 μl of sperm (from 3 different
238 animals) in 1 ml of MFSW pH 9.2 for 30 minutes. Activated sperm was added to the eggs at a
239 ratio of approximately 10 μl of sperm to 5-20 eggs for small cultures or injected eggs, and 100
240 μl for 10 ml of MFSW for large cultures. Following fertilization eggs were transferred to a fresh
241 dish to remove excess sperm.
242

243 **Plasmids and RNAs**

244 Plasmids encoding NLS-3Venus, NLS-tomato, PH-tomato and PH-GFP were
245 previously described (McDougall et al., 2015). Following plasmid linearization with Sfi1,
246 RNAs were synthetized using T3 RNA polymerase (mMessage-mMachine kit, Invitrogen).
247 NLS-3Venus and NLS-tomato RNAs were injected in unfertilized eggs at the concentration of
248 4 μg/μl. PH-tomato and PH-GFP were injected in unfertilized eggs at a concentration of 1 μg/μl.
249 At these concentrations, these RNAs did not delay mitotic progression and had no effect on
250 embryonic development.
251 The cDNA encoding Mad2-DN, a phosphomimic form of the human Mad2 that acts as
252 a dominant negative, was provided by Dr K. Wassmann (Wassmann et al., 2003a) and was
253 cloned into the plasmid pCS2 to allow RNA synthesis using SP6 RNA polymerase (mMessage-
254 mMachine kit, Invitrogen, Carlsbad, USA). Following in vitro transcription, a poly(A) tail was
255 added using a polyA-tailing kit (Invitrogen). The Mad2-DN RNA was injected into unfertilized
256 eggs at a concentration of 8 μg/μl.
257 FoxA-a identified as Phmamm.g00001891 (Brozovic et al., 2018) was amplified from
258 a cDNA template using the primers: forward cgcTGTACAAGATGATGTTGTCGTCTCCC
259 and reverse cgcTGTACATTAGTTGGCCGGTACGCA. The FoxA-a coding sequence was
260 used to replace the RFA cassette in pSP72BSSPE-pFog::Venus-RFA provided by Patrick
261 Lemaire (Roure et al., 2007) by enzymatic digestion using BsrGI. The pFog>FoxA-a plasmid
262 was injected at a concentration of 35 ng/μl.
263

264 **Microinjection**

265 Microinjection of unfertilized eggs was carried out as previously described (Yasuo and
266 McDougall, 2018). Briefly glass capillaries without filament (GC100 T10, Harvard Apparatus)
267 were used to store the RNA to be injected. Prior to loading, the RNA solution was centrifuged

268 at 13000 rpm at 10°C for 10 min to pellet impurities that could block the needle. Capillaries
269 (GC100T10 Harvard Apparatus) were cut to 1cm length and filled sequentially with 2 μl of
270 mineral oil, 0.5-1.5 μl RNA or DNA solution and finally 1 μl of mineral oil and kept at 4°C for
271 several weeks.

272 Injections were performed using a Leica DM IL LED inverted microscope (10x
273 objective) in transmitted light. Needles were made by pulling capillaries with a Narishige
274 horizontal puller (PN-30). The needle was attached to a NarishigeIM300 injection box and
275 manipulated using a three-axis hydraulic micromanipulator (Narishige MMO-203 associated
276 with NarishigeNO-SIX-2 mounting adaptor and Narishige HI-7 pipette holder). Eggs were
277 immobilized in horizontal injection chambers (Yasuo and McDougall, 2018) filled with MFSW
278 and injected to 5% of their volume.
279

280 **Pole ablation**

281 Following fertilization, the cytoplasm of ascidian embryos undergoes significant
282 rearrangements that lead to the localization of many maternal factors into a transient surface
283 protrusion known as the contraction pole (Nishida, 1994; Nishida, 1996). Ablation of this pole
284 was performed by aspiration with a micropipette as previously described (Nishida, 1996). An
285 aspiration micropipette, formed by breaking the tip of a microinjection needle to obtain a blunt
286 opening, was connected to a mouth pipette. Eggs were fertilized in a petri dish and immediately
287 transferred into an injection chamber mounted on an inverted microscope as for microinjection.
288 The contraction pole was aspirated into the pipette by suction and a quick movement of the
289 needle perpendicularly to the egg surface sealed the membrane of the zygote. Eggs were then
290 transferred to a new dish to allow development.
291

292 **Drug treatments**

293 All drugs were stored in small aliquots at -20°C.

294 Nocodazole (Sigma-Aldrich, St. Louis, MO, USA) was resuspended in DMSO to obtain
295 a 33 mM stock solution and was used at a final concentration of 10 μM in MFSW. Reversine
296 (Axon Medchem, Groningen, The Netherlands) was resuspended in DMSO at 5 mM and used
297 at a final concentration of 0.5 μM in MFSW. Both drugs were added to MFSW when embryos
298 reached the analyzed stage and embryos were then maintained in the presence of the drug for
299 the duration of the experiment.

300 BIO ((2'Z,3'E)-6-Bromoindirubin-3'oxime, Millipore) was resuspended in DMSO to
301 obtain a 10 mM stock solution and was then used at a final concentration of 2.5 μM in MFSW.
302 Embryos were soaked in 2.5 μM BIO, in the dark, from the onset of gastrulation (stage 10,
303 about 5hpf). Two hours later (about 7 hpf) embryos were treated with 10μM nocodazole and
304 maintained in the presence of both drugs for the remaining of the experiment.
305

306 **Immunofluorescence**

307 For immunofluorescence, embryos were collected at the required stage and fixed
308 overnight in 100% methanol at -20°C. For Mad1 staining, embryos were treated with 10μM
309 nocodazole before fixation. After fixation, embryos were washed 3 times in PBS containing
310 0.1% triton-X-100 (PBST), then incubated in PBST containing 3% BSA (PBST-BSA) for 1
311 hour at room temperature (RT) and finally incubated overnight at 4°C in PBST-BSA with the
312 anti-tubulin antibody, DM1A (mouse, Sigma-Aldrich) at 1:500 dilution or a specific antibody
313 raised against *P. mammillata* Mad1 at 1:100 dilution (Chenevert et al., 2020). After overnight
314 incubation, excess antibody was removed by 3 consecutive washes in PBST. Embryos were
315 then incubated in PBST-BSA with either Alexa fluor 546 or Alexa fluor 488 anti-mouse
316 secondary antibody (Jackson ImmunoResearch, Ely, UK; 1:1000) at RT for 1-2 hours.
317 Following 2 further washes in PBST, embryos were incubated for 10 minutes in PBST
318 containing Hoechst 33342 (5 μg/ml), washed twice and then mounted in citifluor AF1 (Science
319 Services, München, Germany), for imaging with a Leica SP8 inverted confocal microscope
320 using a 40x water objective.
321

322 **Time-Lapse Microscopy**

323 For live imaging, embryos were mounted between GF coated slide and coverslip, using
324 Dow Corning vacuum grease as spacer. In early stages (2- to 16-cell embryos) nuclei were
325 followed by brightfield microscopy while at later stages (32-512 cell) we relied on the
326 localization of a fluorescent protein, Venus or Tomato, fused to a nuclear localization signal
327 (NLS-3Venus or NLS-Tomato). The NLS protein accumulates in the nucleus during interphase,
328 while from NEB to NER (mitosis) the signal disperses in the cytoplasm. To distinguish
329 individual cells within the embryo, eggs were co-injected with an mRNA encoding the plasma-
330 membrane marker PH domain-GFP. Following fertilization embryos were maintained in
331 MFSW until they reached the stage of interest and then treated with the different drugs
332 (nocodazole, reversine, BIO) or DMSO and transferred to the appropriate microscope for

333 recording. Live imaging was always performed in a temperature-controlled room set at 19°C.
334 When possible, control and treated embryos were imaged in parallel on the same microscope.
335 Image acquisition was performed on the Plateforme d'Imagerie Microscopique de
336 Villefranche (PIM). For brightfield imaging, a z-stack covering the entire embryo with a z step
337 of 2 μm was acquired using a Zeiss (Oberkochen, Germany) Axiovert 100 or Axiovert 200
338 inverted microscope with bright field optics fitted with a 40x/1.1NA objective and equipped
339 with a CoolSnap Kino camera (Photometrics) and Metamorph acquisition software. Images
340 were acquired every 1-2 minutes. For NLS expressing embryos, a z-stack covering the entire
341 embryo with a z step of 2 μm was acquired using a Leica (Wetzlar, Germany) SP8 inverted
342 confocal microscope fitted with a 40x water immersion objective and 408, 488, and 552 nm
343 lasers and the Leica application suite acquisition software (LASX). Images were acquired every
344 2 minutes.
345

346 **Image analysis**

347 Images were analyzed using different softwares: Metamorph (Molecular Devices, San
348 Jose, USA), imageJ-Fiji (Schindelin et al., 2012), Imaris (Imaris, BitPlane, Zurich, Switzerland)
349 and Icy (de Chaumont et al., 2012) with the plugin Z-explorer
350 (https://icy.bioimageanalysis.org/plugin/z-explorer/). Presence or absence of nuclei was
351 determined manually by following each cell over time through the entire Z stack. At the 512-
352 cell stage, if a cell did not exit mitosis for more than 1 hour before the end of acquisition, we
353 assigned a mitotic duration of 60 minutes. Approximate cell number was assessed by counting
354 number of nuclei using the Spot tool in Imaris. Cell volume was determined using the Surface
355 tool in Imaris: the cell contour was drawn in each frame based on the signal from the plasma-
356 membrane associated PH-GFP or PH-Tomato, the reconstructed cell shape was confirmed
357 using 3D visualization of the embryo and then the cell volume was retrieved.
358

359 **Western blot**

360 To assess Mad1 levels, 30 eggs or embryos were collected for each stage from egg to
361 512-cell stage. Embryos were collected in MFSW and mixed with the same volume of 2x
362 Laemmli (100 mM Tris-HCl at pH 6.8, 4% SDS, 0.2 % bromophenol blue, 20 % glycerol, 200
363 mM dithiothreitol). Samples were heated for 5 minutes at 95°C and then kept at -20°C. Samples
364 were separated on a 10% SDS-polyacrylamide gel and then transferred to a nitrocellulose
365 membrane. Membranes were blocked for 1h in Tris Buffer-Saline (TBS: 20mM Tris Base, 150

366 mM NaCl) containing 2% milk, 0.1% tween-20 (TBS-Tween-milk) and then incubated in
367 blocking solution containing the appropriate antibody overnight at 4°C. For Mad1 detection
368 the Mad1 antibody (Chenevert et al., 2020) was diluted 1:2000, whereas for tubulin detection,
369 the DM1a antibody (Sigma-Aldrich, mouse) was diluted 1:3000. Following antibody
370 incubation, membranes were washed 3 times with TBS-Tween (TBS with 0.1% tween-20) and
371 incubated with an appropriate horseradish peroxidase-conjugated secondary antibody (Jackson
372 ImmunoResearch) at 1:10000 dilution in TBS-Tween-milk for 1 hour at RT. After 3 washes
373 with TBS-Tween, signal detection was carried out using the SuperSignal West Pico chemio-
374 luminescent substrate (Thermo Scientific, Waltham, MA, USA) as described by the
375 manufacturer and imaged in the Vilmen-Loubet Fusion machine.
376

377 ***In situ* hybridization**

378 The *sFRP1/5* sequence identified as Phmamm.g0000599 (Brozovic et al., 2018) and the
379 *FoxF* sequence identified as Phmamm.g07919 were amplified from cDNA templates. After
380 linearization by enzymatic digestion with SalI, an *in situ* hybridization probe covering the
381 coding sequence, was generated by in vitro transcription using T7 RNA polymerase (Promega,
382 Charbonnières-les-Bains, France) in presence of Digoxygenin-labeled nucleotides (DIG RNA
383 Labeling Mix, Roche, Bâle, Switzerland).

384 *In situ* hybridization experiments were performed as previously described (Paix et al.,
385 2009). Eggs and embryos were fixed overnight at 4°C in 4% formaldehyde, 100 mM MOPS,
386 0.5 M NaCl, pH 7.6, washed 3 times in PBS, progressively dehydrated in ethanol (25%, 50%,
387 75%, 100%) and stored at –20°C. Fixed eggs and embryos were then re-hydrated by addition
388 of an equal volume of PBS/0.1% Tween 20 (PBSTw), washed once in PBSTw and then
389 incubated with 2 µg/ml proteinase K (Sigma) in PBSTw for 25 minutes at room temperature
390 (RT). After 3 washes in PBSTw, embryos were fixed again in PBS containing 4% formaldehyde
391 (1 h, RT) and washed again to remove formaldehyde. Embryos were then incubated in
392 hybridization buffer (50% formamide, 6× saline sodium citrate (SSC), 5× Denhardt's solution,
393 1 mg/ml yeast RNA, 0.1% Tween, pH = 7.5) for 1 h at 65 °C. Probes were added to fresh
394 hybridization solution at a final concentration of 0.5 ng/µl and hybridization was performed
395 overnight at 65°C. After hybridization, embryos were washed at 65°C twice in 50% formamide,
396 5× SSC, 1% SDS (30 min), twice in 50% formamide, 2× SSC, 1% SDS (15 min), once in 2×
397 SSC, 0.1% Tween (15 min) and twice in 0.2× SSC, 0.1% Tween (15 min). All solutions were
398 at pH 7.5. Embryos were then incubated in blocking buffer (0.15 M NaCl, 0.5% BBR, 0.1M

399 Tris pH8) for 1h at RT. Anti-DIG AP antibody (Roche, Bâle, Switzerland, 1:4000) was added
400 in fresh blocking solution and incubated at 4 °C overnight. After incubation, embryos were
401 washed 5 times in PBSTw (3 times for 10 min, 30 min, 1 h respectively) and then in TBSTw at
402 4°C overnight. Embryos were washed once with reaction buffer (0.1 M Tris pH 9.5, 50 mM
403 $MgCl_2$, 0.1M NaCl, 0.1% Tween) and then the detection reaction was carried out in a buffer
404 containing 3.5 μl/ml of of nitro blue tetrazolium (NBT) and 5-bromo-4-chloro-3-indolyl-
405 phosphate (BCIP) (Roche, Bâle, Switzerland). The reaction was stopped with 50 mM EDTA in
406 PBS and embryos were washed in PBSTw. Embryos were fixed in 4% formaldehyde in PBS,
407 washed in PBS and mounted in 80% Glycerol. Stained embryos were imaged using an optical
408 microscope (Zeiss Imager A2) equipped with a xxx camera and Zeiss Zen blue software, using
409 a 20x objective.
410

411 **Quantification and statistical analysis**

412 Number of analyzed embryos (N) and cells (n) are reported under each graph. For each
413 experiment at least 3 independent biological repeats were included. For statistical analysis the
414 non-parametric test of Wilcoxon-Mann-Whitney was applied. For all comparisons, we used
415 population medians as the mean can be affected by extreme values and is highly impacted by
416 outliers (Gaddis and Gaddis, 1990). However, means and standard deviations are also provided
417 in the text. Statistical tests and graphics were performed using the R software (R Core Team,
418 2016) and the library "pretty R" (Grosjean and Lemon, 2015) was used to retrieve median,
419 mean and standard deviation.

420 Box plot represents the distribution of the data using quartiles (Q). Q1, Q2 and Q3 being
421 respectively the values below which lie 25%, 50% and 75% of the data points. Q1 and Q3 form
422 the limits of the box and the median Q2 is indicated by a bolder line. The whiskers represent
423 the range in which most values are found, whereas the values outside represent the outliers.
424

425 **Acknowledgments**

426 We are grateful to E. Houliston, H. Yasuo, C. Hudson, S. Darras, R. Dumollard, P. Lemaire
427 and K. Wassmann for discussion, sharing of reagents or critical reading of the manuscript.
428 We would also like to thank C. Hebras, F. Bekkouche, L. Gilletta, M. Temagoult, S. Benaicha,
429 and S. Schaub for technical assistance. We thank the Service Aquarologie of CRB (IMEV-
430 FR3761) for access to marine facilities and animals and the microscopy platform PIM (member

of the MICA microscopy platform) where image acquisition was conducted. CRB and PIM are supported by EMBRC-France, whose French state funds are managed by the ANR within the investments for the future program under reference ANR-10-INSB-02.
This research was funded by the CNRS and from PACA region (project Mepanep, 2014_03738).

Competing interests

The authors declare no competing interests.

References

Brozovic, M., Dantec, C., Dardaillon, J., Dauga, D., Faure, E., Gineste, M., Louis, A., Naville, M., Nitta, K. R., Piette, J., et al. (2018). ANISEED 2017: extending the integrated ascidian database to the exploration and evolutionary comparison of genome-scale datasets. *Nucleic Acids Res*. 46, D718–D725.

Chenevert, J., Roca, M., Besnardeau, L., Ruggiero, A., Nabi, D., McDougall, A., Copley, R. R., Christians, E. and Castagnetti, S. (2020). The Spindle Assembly Checkpoint Functions during Early Development in Non-Chordate Embryos. *Cells* 9,.

Chunduri, N. K. and Storchová, Z. (2019). The diverse consequences of aneuploidy. *Nat. Cell Biol*. 21, 54–62.

Clute, P. and Masui, Y. (1995). Regulation of the appearance of division asynchrony and microtubule-dependent chromosome cycles in Xenopus laevis embryos. *Dev. Biol.* 171, 273–285.

Clute, P. and Masui, Y. (1997). Microtubule dependence of chromosome cycles in Xenopus laevis blastomeres under the influence of a DNA synthesis inhibitor, aphidicolin. *Dev. Biol*. 185, 1–13.

De Antoni, A., Pearson, C. G., Cimini, D., Canman, J. C., Sala, V., Nezi, L., Mapelli, M., Sironi, L., Faretta, M., Salmon, E. D., et al. (2005). The Mad1/Mad2 Complex as a Template for Mad2 Activation in the Spindle Assembly Checkpoint. *Curr. Biol*. 15, 214–225.

459 de Chaumont, F., Dallongeville, S., Chenouard, N., Hervé, N., Pop, S., Provoost, T., Meas-
460 Yedid, V., Pankajakshan, P., Lecomte, T., Le Montagner, Y., et al. (2012). Icy: an
461 open bioimage informatics platform for extended reproducible research. *Nat. Methods*
462 9, 690–696.

463 Dumollard, R., Minc, N., Salez, G., Aicha, S. B., Bekkouche, F., Hebras, C., Besnardeau, L.
464 and McDougall, A. (2017). The invariant cleavage pattern displayed by ascidian
465 embryos depends on spindle positioning along the cell's longest axis in the apical
466 plane and relies on asynchronous cell divisions. *eLife* 6, e19290.

467 Feinberg, S., Roure, A., Piron, J. and Darras, S. (2019). Antero-posterior ectoderm patterning
468 by canonical Wnt signaling during ascidian development. *PLOS Genet*. 15, e1008054.

469 Gaddis, G. M. and Gaddis, M. L. (1990). Introduction to biostatistics: Part 2, Descriptive
470 statistics. *Ann. Emerg. Med.* 19, 309–315.

471 Galli, M. and Morgan, D. O. (2016). Cell size determines the strength of the spindle assembly
472 checkpoint during embryonic development. *Dev. Cell* 36, 344–352.

473 Gerhold, A. R., Poupart, V., Labbé, J.-C. and Maddox, P. S. (2018). Spindle assembly
474 checkpoint strength is linked to cell fate in the Caenorhabditis elegans embryo. *Mol.*
475 *Biol. Cell* 29, 1435–1448.

476 Grosjean, P. and Lemon (2015). prettyR: Pretty Descriptive Stats.

477 Jia, L., Kim, S. and Yu, H. (2013). Tracking spindle checkpoint signals from kinetochores to
478 APC/C. *Trends Biochem. Sci.* 38, 302–311.

479 Kyogoku, H. and Kitajima, T. S. (2017). Large Cytoplasm Is Linked to the Error-Prone
480 Nature of Oocytes. *Dev. Cell* 41, 287-298.e4.

481 Lamy, C., Rothbächer, U., Caillol, D. and Lemaire, P. (2006). Ci-FoxA-a is the earliest
482 zygotic determinant of the ascidian anterior ectoderm and directly activates Ci-
483 sFRP1/5. *Development* 133, 2835–2844.

484 Lane, S. I. R., Morgan, S. L., Wu, T., Collins, J. K., Merriman, J. A., ElInati, E., Turner, J. M.
485 and Jones, K. T. (2017). DNA damage induces a kinetochore-based ATM/ATR-

486 independent SAC arrest unique to the first meiotic division in mouse oocytes. *Dev. Camb. Engl.* 144, 3475–3486.

488 McDougall, A., Chenevert, J., Pruliere, G., Costache, V., Hebras, C., Salez, G. and Dumollard, R. (2015). Chapter 17 - Centrosomes and spindles in ascidian embryos and eggs. In *Methods Cell Biol.* (ed. Basto, R.) and Oegema, K.), pp. 317–339. Academic Press.

492 Minshull, J., Sun, H., Tonks, N. K. and Murray, A. W. (1994). A MAP kinase-dependent spindle assembly checkpoint in Xenopus egg extracts. *Cell* 79, 475–486.

494 Musacchio, A. and Salmon, E. D. (2007). The spindle-assembly checkpoint in space and time. *Nat. Rev. Mol. Cell Biol.* 8, 379–393.

496 Nishida, H. (1994). Localization of determinants for formation of the anterior-posterior axis in eggs of the ascidian Halocynthia roretzi. *Development* 120, 3093–3104.

498 Nishida, H. (1996). Vegetal egg cytoplasm promotes gastrulation and is responsible for specification of vegetal blastomeres in embryos of the ascidian Halocynthia roretzi. *Development* 122, 1271–1279.

501 Paix, A., Yamada, L., Dru, P., Lecordier, H., Pruliere, G., Chenevert, J., Satoh, N. and Sardet, C. (2009). Cortical anchorages and cell type segregations of maternal postplasmic/PEM RNAs in ascidians. *Dev. Biol.* 336, 96–111.

504 R Core Team, R. C. T. (2016). R: A Language and Environment for Statistical Computing.

505 Rashid, M. S., Mazur, T., Ji, W., Liu, S. T. and Taylor, W. R. (2018). Analysis of the role of GSK3 in the mitotic checkpoint. *Sci. Rep.* 8,.

507 Rodriguez-Bravo, V., Maciejowski, J., Corona, J., Buch, H. K., Collin, P., Kanemaki, M. T., Shah, J. V. and Jallepalli, P. V. (2014). Nuclear pores protect genome integrity by assembling a premitotic and Mad1-dependent anaphase inhibitor. *Cell* 156, 1017–1031.

511 Roure, A., Rothbächer, U., Robin, F., Kalmar, E., Ferone, G., Lamy, C., Missero, C., Mueller, F. and Lemaire, P. (2007). A Multicassette Gateway Vector Set for High Throughput and Comparative Analyses in Ciona and Vertebrate Embryos. *PLoS ONE* 2,.

514 Santaguida, S., Tighe, A., D'Alise, A. M., Taylor, S. S. and Musacchio, A. (2010). Dissecting
515 the role of MPS1 in chromosome biorientation and the spindle checkpoint through the
516 small molecule inhibitor reversine. *J. Cell Biol.* 190, 73–87.

517 Sardet, C., Speksnijder, J., Inoue, S. and Jaffe, L. (1989). Fertilization and ooplasmic
518 movements in the ascidian egg. *Dev. Camb. Engl.* 105, 237–249.

519 Schindelin, J., Arganda-Carreras, I., Frise, E., Kaynig, V., Longair, M., Pietzsch, T.,
520 Preibisch, S., Rueden, C., Saalfeld, S., Schmid, B., et al. (2012). Fiji: an open-source
521 platform for biological-image analysis. *Nat. Methods* 9, 676–682.

522 Sudakin, V., Chan, G. K. T. and Yen, T. J. (2001). Checkpoint inhibition of the APC/C in
523 HeLa cells is mediated by a complex of BUBR1, BUB3, CDC20, and MAD2. *J. Cell*
524 *Biol.* 154, 925–936.

525 Vázquez-Diez, C., Paim, L. M. G. and FitzHarris, G. (2019). Cell-Size-Independent Spindle
526 Checkpoint Failure Underlies Chromosome Segregation Error in Mouse Embryos.
527 *Curr. Biol.* 29, 865-873.e3.

528 Wassmann, K., Liberal, V. and Benezra, R. (2003a). Mad2 phosphorylation regulates its
529 association with Mad1 and the APC/C. *EMBO J.* 22, 797–806.

530 Wassmann, K., Niault, T. and Maro, B. (2003b). Metaphase I arrest upon activation of the
531 Mad2-dependent spindle checkpoint in mouse oocytes. *Curr. Biol. CB* 13, 1596–1608.

532 Yasuo, H. and McDougall, A. (2018). Practical Guide for Ascidian Microinjection: Phallusia
533 mammillata. *Adv. Exp. Med. Biol.* 1029, 15–24.

534 Zhang, M., Kothari, P. and Lampson, M. A. (2015). Spindle assembly checkpoint acquisition
535 at the mid-blastula transition. *PloS One* 10, e0119285.

536

537

538

539

Figures

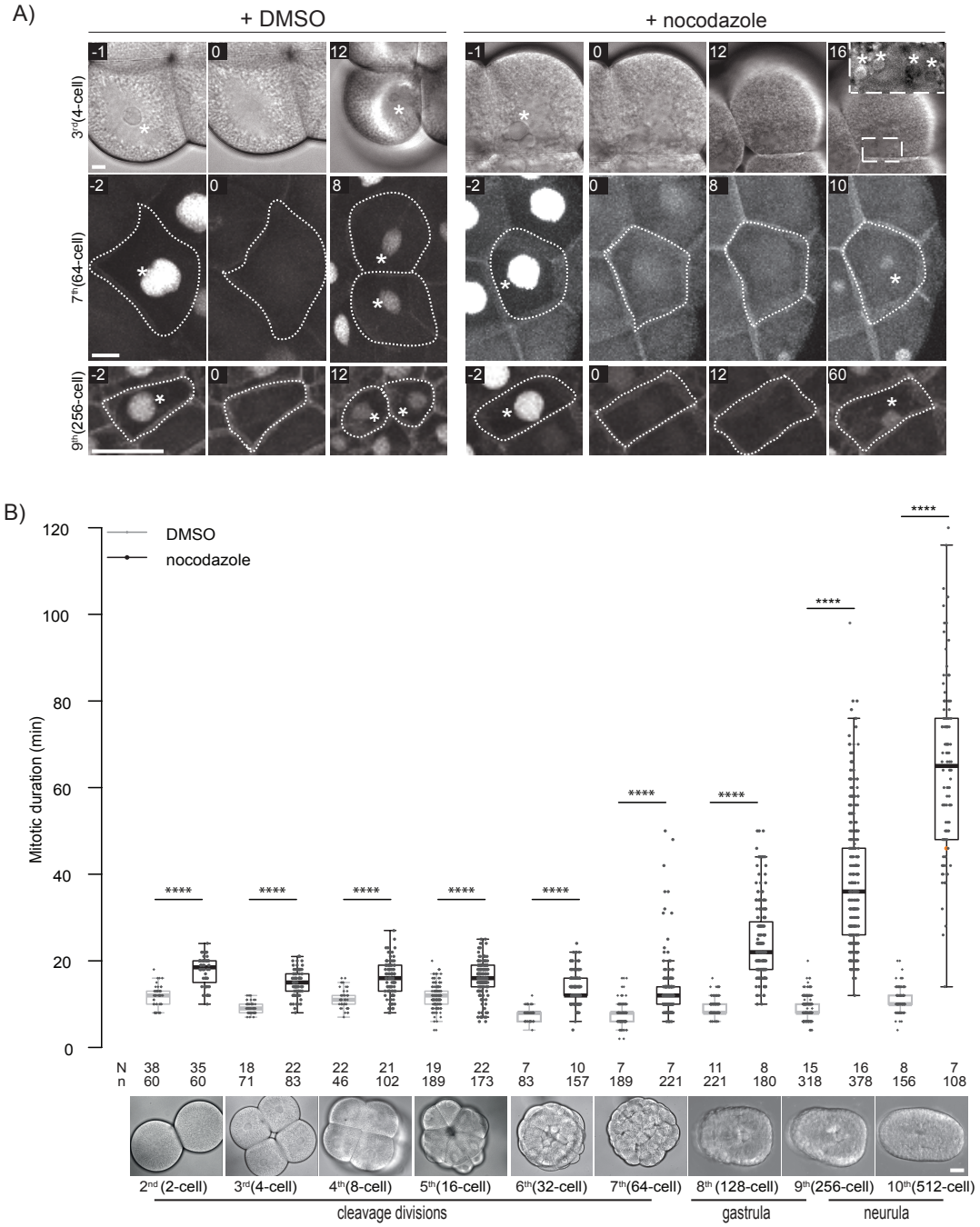

Figure 1

543 **Figure 1: Nocodazole treatment induces a prolonged delay in mitotic progression from**
544 **the 8th cell cycle**.

545 **A)** Representative images of cells from 4- (top), 64- (middle) and 256-cell (bottom) embryos
546 treated with DMSO (left) or with nocodazole (right). Asterisks indicate nuclei. NEB is
547 considered as time 0 and time before or after NEB (minutes) is indicated on each image. See
548 also Movies 1 and 2. Dotted lines indicate cell periphery. Fluorescence images are projections
549 of the confocal Z-stack covering the whole cell. **B)** Quantification of mitotic duration in DMSO
550 (grey) or nocodazole (black) treated embryos from 2nd to 10th cell cycle (2- to 512-cell).
551 Representative brightfield images of *P. mammillata* embryos are presented below the plot for
552 all analyzed stages. Each dot represents a cell. Boxes represent 25-75th percentiles, and the
553 median is shown. Number of analyzed embryos (N) and cells (n) is given for each stage. Test
554 of Wilcoxon-Mann-Whitney performed using all cells: non-significant (ns), p-value ≤ 0.05 (*),
555 ≤ 0.01 (**), ≤ 0.001 (***), ≤ 0.0001 (****). Scale bars are 10 μm in A and 30 μm in B.

556

557

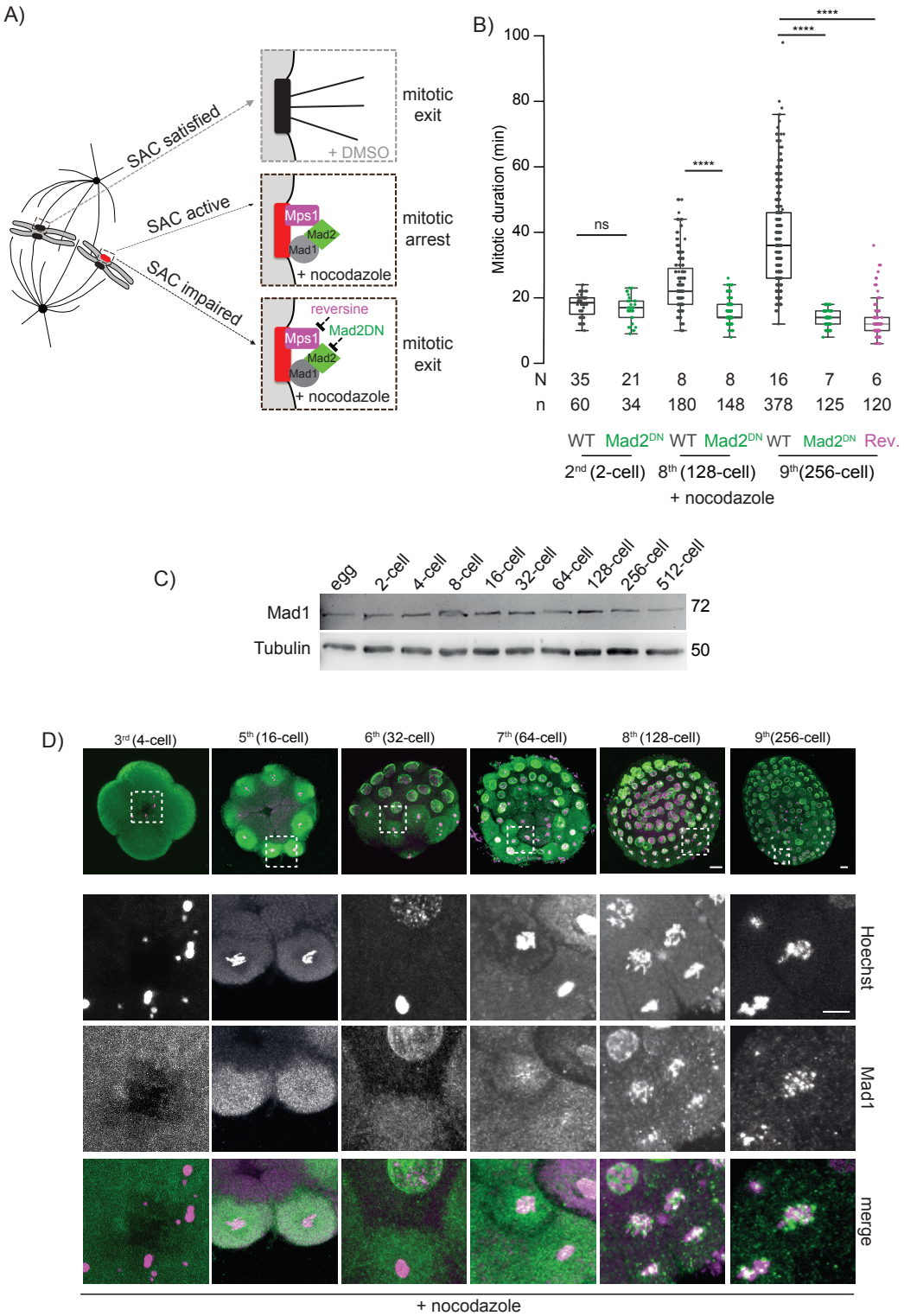
A)
SAC satisfied
SAC active
SAC impaired
mitotic exit
+ DMSO
mitotic arrest
Mps1
Mad2
Mad1
+ nocodazole
reversine
Mad2DN
mitotic exit
B)
Mitotic duration (min)
ns
****
N 35 21 8 8 16 7 6
n 60 34 180 148 378 125 120
WT Mad2DN WT Mad2DN WT Mad2DN Rev.
2nd (2-cell) 8th (128-cell) 9th(256-cell)
+ nocodazole
C)
egg 2-cell 4-cell 8-cell 16-cell 32-cell 64-cell 128-cell 256-cell 512-cell
Mad1
Tubulin
72
50
D)
3rd (4-cell) 5th (16-cell) 6th (32-cell) 7th (64-cell) 8th (128-cell) 9th(256-cell)
Hoechst
Mad1
merge
+ nocodazole

Figure 2

561 **Figure 2: SAC activity is acquired at the 8th cell cycle.**

562 **A)** Schematic representation of mitotic chromosomes and their association with spindle
563 microtubules. SAC proteins Mps1, Mad1 and Mad2 localize to an unattached kinetochore,
564 leading to SAC activation and inhibition of APC/C activity (top). Treatment with the Mps1
565 inhibitor reversine or overexpression of Mad2-DN impairs SAC activity resulting in premature
566 mitotic exit (bottom). **B)** Quantification of mitotic duration in nocodazole treated embryos at
567 2-, 128- and 256-cell stage in wild-type embryos (black) or following SAC impairment by either
568 overexpression of Mad2-DN (green) or treatment with reversine (magenta). Box plots are as in
569 Figure 1B. See also Movies 3 and 4. **C)** Western blot analysis of Mad1 protein (top) throughout
570 development (egg to 512-cell). Tubulin is used as loading control (bottom). **D)** Representative
571 images of 4-, 16-, 32-, 64-, 128- and 256-cell (left to right) embryos treated with nocodazole,
572 stained with Hoechst (DNA, magenta) and for Mad1 (green). White squares indicate mitotic
573 cells enlarged underneath each image. See also Figure S2. Scale bars are 10 μm.

574

575

576

577

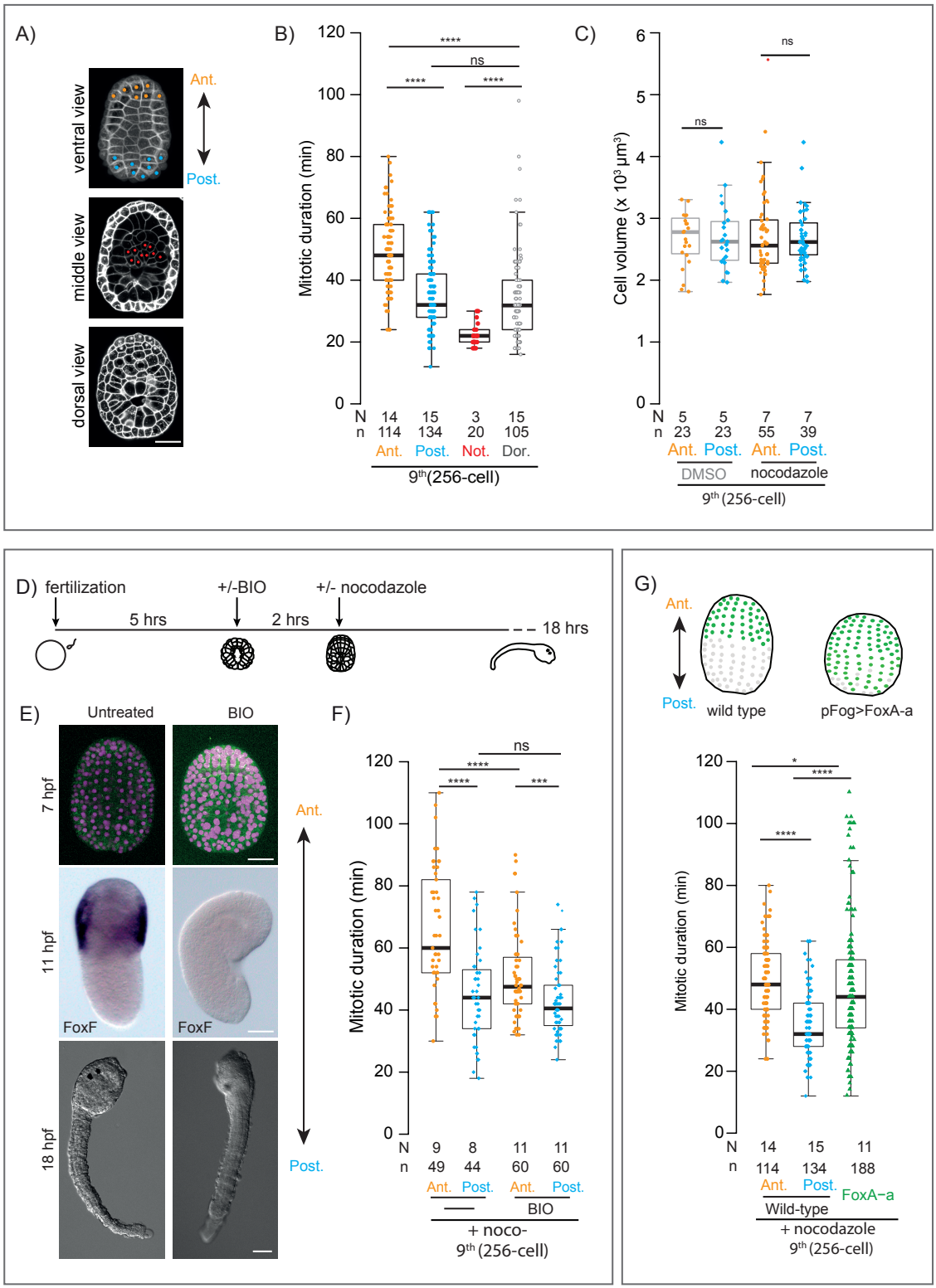

Figure 3

578

579

580

581 **Figure 3: SAC is stronger in anterior ectodermal cells.**

582 **A**) Ventral, middle and dorsal views of cell mask stained 256-cell stage embryo, indicating
583 areas where mitotic duration was analyzed: ventral anterior (orange) and posterior (blue)
584 ectoderm, notochord (red) and dorsal ectoderm (grey). **B)** Mitotic duration in ventral anterior
585 ectoderm (orange), ventral posterior ectoderm (blue), notochord (red) and dorsal cells (grey) of
586 nocodazole treated wild type 256-cell stage embryos. **C)** Cell volume of ventral anterior
587 (orange) and posterior (blue) ectodermal cells in 256-cell stage embryos in the presence of
588 either DMSO (grey) or nocodazole (black). **D)** Schematic representation of experiment to
589 analyze impact of GSK3 activity on mitotic duration. **E)** Representative images of control (left)
590 and BIO-treated (right) 256-cell stage embryos (7 hours post fertilization, hpf), expressing
591 NLS-Tomato (magenta) and PH-GFP (green), early tailbud embryos (11hpf) showing the
592 expression pattern of the anterior marker *FoxF* and tadpoles (18 hpf). **F)** Mitotic duration in
593 ventral anterior (orange) and posterior (blue) ectodermal cells of control (DMSO) embryos and
594 BIO-treated embryos at the 9th cell cycle in the presence of nocodazole. Box plot in C is as in
595 Figure 1B. **G)** Top: schematic representation of FoxA-a expression (green) in wild type and
596 pFog>FoxA-a over-expressing embryos. Bottom: mitotic duration in ventral anterior ectoderm
597 (orange), ventral posterior ectoderm (blue) and pFog>FoxA-a overexpressing embryos (green)
598 at the 9th cell cycle in the presence of nocodazole. Scale bars are 30μm.
599
600
601

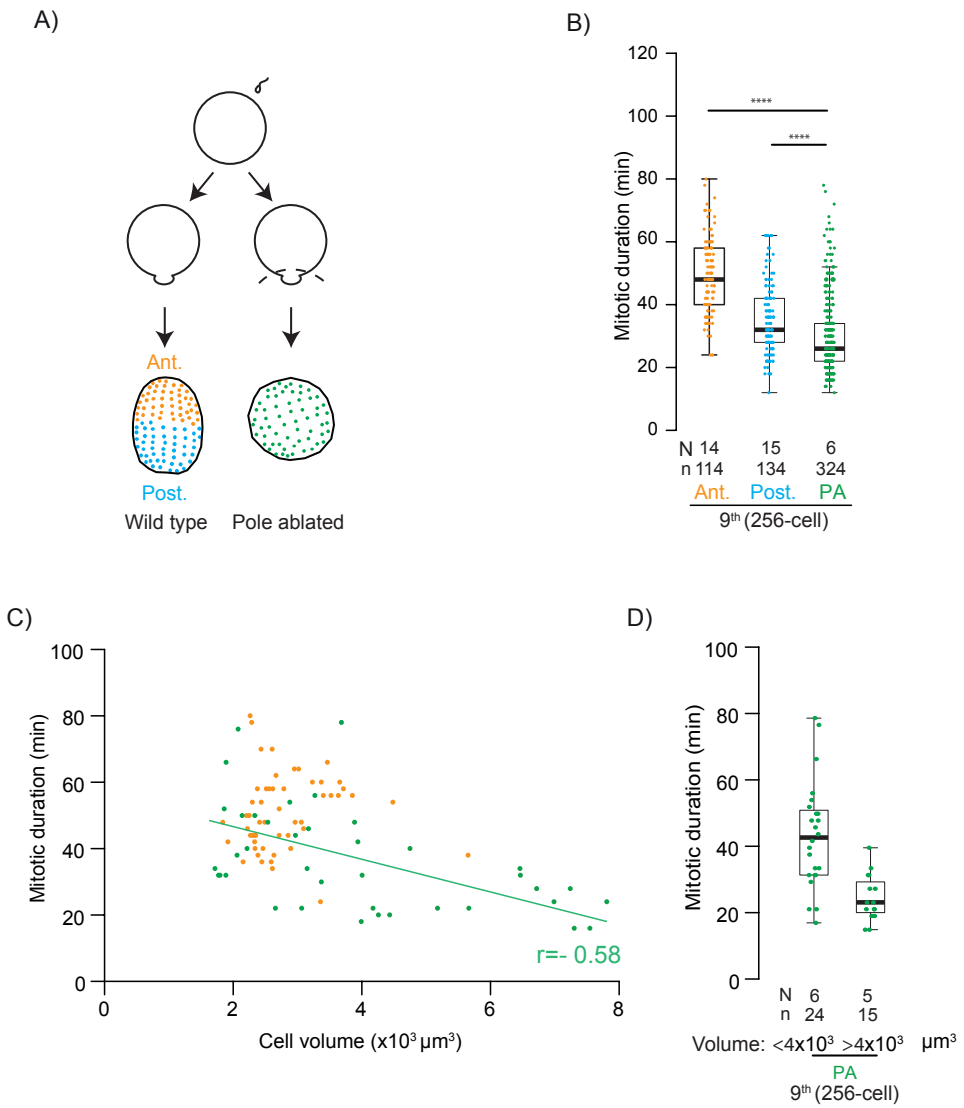

Figure 4

602

603

604

605 **Figure 4: SAC strength depends on cell size.**

606 **A)** Schematic representation of non-manipulated (left) and pole-ablated (right) fertilized eggs
607 and resultant embryos. **B)** Mitotic duration in the presence of nocodazole for wild type ventral
608 anterior (orange) and posterior (blue) ectodermal cells and cells from pole-ablated embryos
609 (green) at the 9th cell cycle. **C)** Mitotic duration in pole-ablated embryos and anterior ectodermal
610 cells treated with nocodazole as a function of cell volume at the 9th cell cycle. The line indicates
611 the regression fit for pole ablated cells and r the coefficient of correlation for the two variables
612 in the same cells. **D)** Mitotic duration in small ($< 4x10^3 \mu m^3$) and large ($> 4x10^3 \mu m3$) cells from
613 nocodazole treated pole-ablated (green) embryos at the 9th cell cycle. For B), C) and D) boxes
614 are as in Figure 1B.

615

616